Supporting Information

Phonon and charge-carrier transport decoupling *via* amorphous carbon coating promotes high thermoelectric cooling performance of p-type $Bi_{0.5}Sb_{1.5}Te_3$

Qiulin Liu,[a,b,1] Qi Zhao,[a,1] Zhen Fan,[a,*] Yi Wang,[a,c] Xiaowei Wu,[a,b] Kaiwei Guo,[a,b] Xuejuan Dong,[a] Hangtian Zhu,[a] and Huaizhou Zhao.[a]

a. Beijing National Laboratory for Condensed Matter Physics, Institute of Physics, Chinese Academy of Sciences, Beijing 100190, China.
b. School of Physical Sciences, University of Chinese Academy of Sciences, Beijing 100049, China.
c. College of Materials Science and Opto-Electronic Technology, University of Chinese Academy of Sciences, Beijing, 100049, China.
1. These authors contributed equally.
* Email: fanzhen@iphy.ac.cn

The Single parabolic model (SPB) calculation

The Seebeck coefficient depends on the reduced Fermi-level in the following equation:

$$S = \pm \frac{k_B}{e}\left(\frac{(r+5/2)F_{r+3/2}(\eta)}{(r+3/2)F_{r+1/2}(\eta)} - \eta\right) \#\ (S1)$$

where $F_i(\eta)$ is the Fermi-Dirac integral:

$$F_i(\eta) = \int_0^\infty \frac{x^i}{1+e^{x-\eta}} dx \#\ (S2)$$

$$n = \frac{4\pi\left(2m^* k_B T\right)^{3/2} F_{1/2}(\eta)}{h^3} \#\ (S3)$$

$$\eta = \frac{E_f}{k_B T} \#\ (S4)$$

The density-of-state effective mass m_{dos}* is determined by the Seebeck data and the carrier concentration.

$$m_{dos}{}^* = \frac{h^2}{2k_B T}\left[\frac{n}{4\pi F_{1/2}(\eta)}\right]^{2/3} \#(S5)$$

The Lorenz factor (L) is calculated as.

$$L = \left(\frac{k_B}{e}\right)^2 \left[\frac{(r+7/2)F_{r+5/2}(\eta)}{(r+3/2)F_{r+1/2}(\eta)} - \left(\frac{(r+5/2)F_{r+3/2}(\eta)}{(r+3/2)F_{r+1/2}(\eta)}\right)^2\right] \#(S6)$$

The electronic conductivity is estimated from the Wiedemann-Franz law:

$$k_e = L\sigma T \qquad (S7)$$

and lattice thermal conductivity is estimated by subtracting k_e from k_{total}.

Calculation of the lattice thermal conductivity

To quantify the effects of the amorphous carbon coating on phonon scattering, the Debye-Callaway model was applied in the pristine BST and BST@C003 samples.[1] The Umklapp phonon-phonon scattering (U), grain boundary scattering (GB), point defect scattering (PD), second phase scattering (SP), and dislocation scattering (DS) were mainly considered. The frequency-dependent phonon scattering was evaluated since phonons carry heat in a broad range of frequencies considering the kinetic theory. The lattice thermal conductivity is described by the following equation:

$$\kappa_{ph} = \frac{k_B}{2\pi^2 v}\left(\frac{k_B T}{\hbar}\right)^3 \int_0^{\theta_D/T} \tau_{tot}(x) \frac{x^4 e^x}{\left(e^x - 1\right)^2} dx \tag{S8}$$

here, v is the average sound speed, k_B is the Boltzmann constant, $\hbar$ is the reduced Plank constant, θ_D is the Debye temperature, and τ_{tot} is the total phonon relaxation time. According to Matthiessen's rule, the total phonon relaxation time (τ_{tot}) is a reciprocal sum of the relaxation times:

$$\tau_{tot}^{-1} = \tau_U^{-1} + \tau_{PD}^{-1} + \tau_{GB}^{-1} + \tau_{DS}^{-1} + \tau_{SP}^{-1} \tag{S9}$$

The Umklapp phonon-phonon scattering (τ_U) is calculated from the equation below:[2]

$$\tau_U^{-1} = A_N \frac{2}{\left(6\pi^2\right)^{1/3}} \frac{k_B V^{1/3} \gamma^2 \omega^2 T}{M v^3} \tag{10}$$

where, V is the atomic volume of matrix, γ is the Grüneisen parameter, T is the absolute temperature, and M is the atomic mass of sample, respectively. A_N is an additional parameter of normal phonon-phonon scattering time.

Point defect scattering is modeled based on the following equation:[3]

$$\tau_{PD}^{-1} = \frac{V\omega^4}{4\pi v^3}\Gamma \tag{S11}$$

$$\Gamma = x(1-x)\left\{\left(\frac{\Delta M}{M}\right)^2 + \frac{2}{9}\left[(G + 6.4\gamma)\frac{1+r}{1-r}\right]^2\left(\frac{\Delta a}{a}\right)^2\right\} \tag{S12}$$

where, x is the fractional concentration of constituents, ΔM is difference in mass, G is

a fractional ratio of bulk modulus, r is Poisson ratio, and Δa is the difference in lattice constant. The relaxation time by grain boundary scattering is given by the following equation:[4]

$$\tau_{GB}^{-1} = \frac{v}{d} \tag{S13}$$

where, d is the average grain size.

The relaxation time for dislocation scattering is given by:[5]

$$\tau_{DS}^{-1} = 0.6B_D^2 N_D(\gamma + \Delta\gamma)^2 \omega \left\{ \frac{1}{2} + \frac{1}{24}\left(\frac{1-2r}{1-r}\right)^2 \left[1 + \sqrt{2}\left(\frac{v_l}{v_t}\right)^2 \right]^2 \right\} + N_D \frac{V^{4/3}}{v^2}\omega^3 \tag{S14}$$

here, N_D, B_D, $\Delta\gamma$, v_l, and v_t represent the dislocation density, the effective Burger's vector, the variation in the Grüneisen parameter, and the longitudinal and transverse phonon velocities, respectively.

The relaxation time for second phase scattering can be described as:[6]

$$\tau_{SP}^{-1} = v\left[\frac{1}{2\pi R^2} + \frac{9}{4\pi R^2}\left(\frac{\rho}{\Delta\rho}\right)^2 \left(\frac{v}{\omega o}\right)^4 \right]^{-1} N_P \tag{S15}$$

where ρ, $\Delta\rho$, o, and N_P denote the mass density of the matrix, the density difference between the matrix and the secondary phase, the average radius of the secondary phase, and the number density of the second phase inclusions, respectively.

In narrow-bandgap thermoelectric semiconductors, bipolar thermal conductivity (κ_{bip}) becomes a non-negligible contribution at elevated temperatures. This arises because high temperatures generate significant concentrations of minority carriers; these carriers absorb heat at the hot side upon excitation and release heat at the cold side upon recombination, thereby introducing an additional heat-transport channel. Accordingly, the total thermal conductivity can be expressed as:[7]

$$\kappa_{tot} = \kappa_e + \kappa_{ph} + \kappa_{bip} \tag{S16}$$

An approximate expression for the bipolar thermal conductivity is given by:[8]

$$\kappa_{bip} = \frac{3L\sigma T}{4\ \pi^2}\left(\frac{E_g}{k_B T} + 4\right) \tag{S17}$$

where L is the Lorenz number and E_g is the bandgap energy.

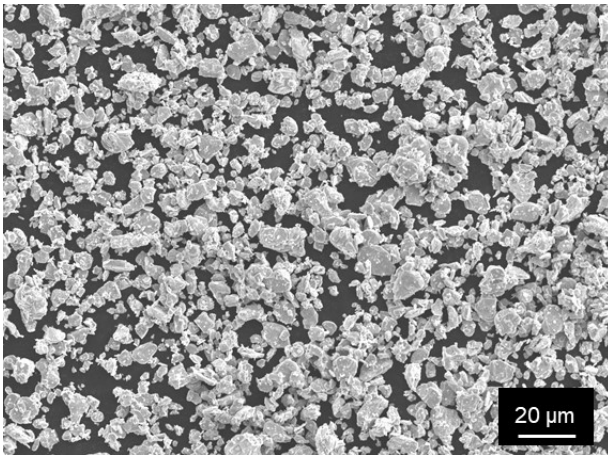

Figure S1. The scanning electron microscopy (SEM) image of pristine BST powders after ball milling.

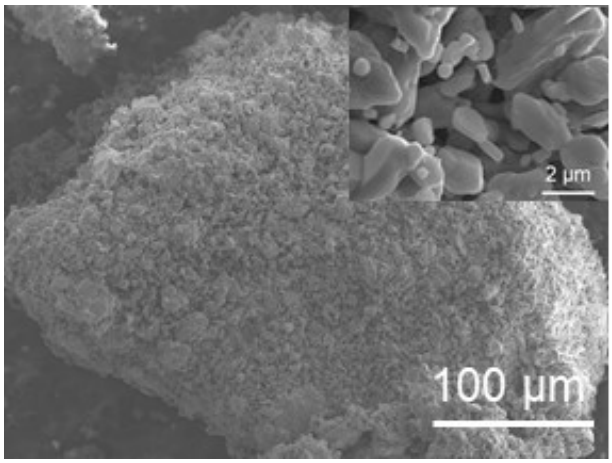

Figure S2. The SEM image of annealing pristine BST powders.

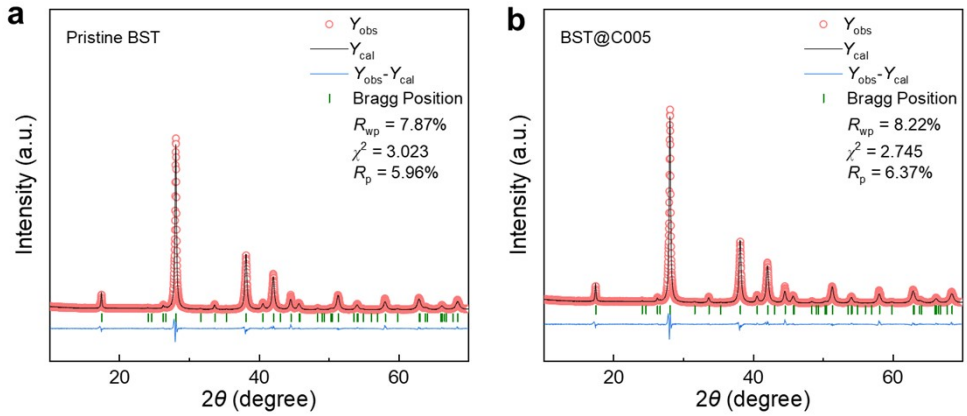

Figure S3. Rietveld refined PXRD of pristine BST, BST@C003, and C005 bulk samples post SPS**.**

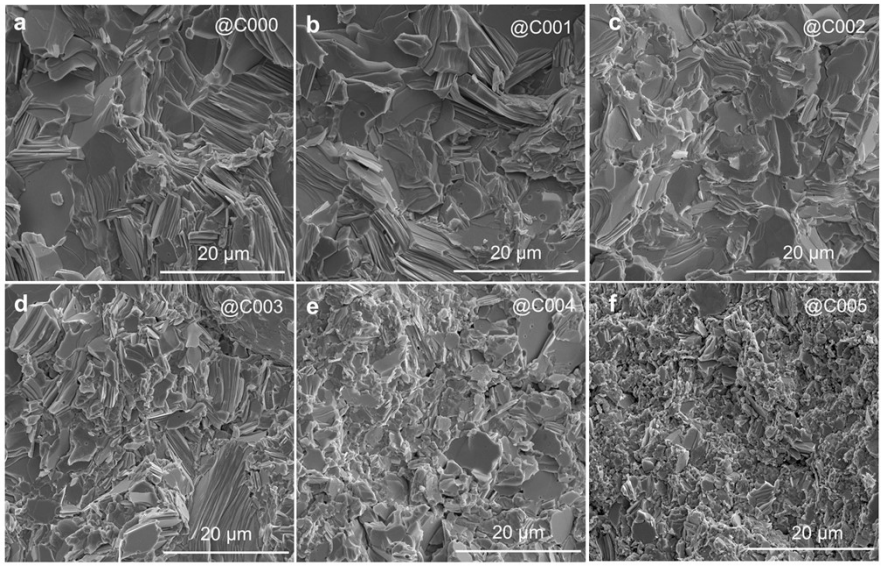

Figure S4. (a-f) SEM images of the fractured surfaces of BST@C000, C001, C002, C003, C004, and C005 bulk samples.

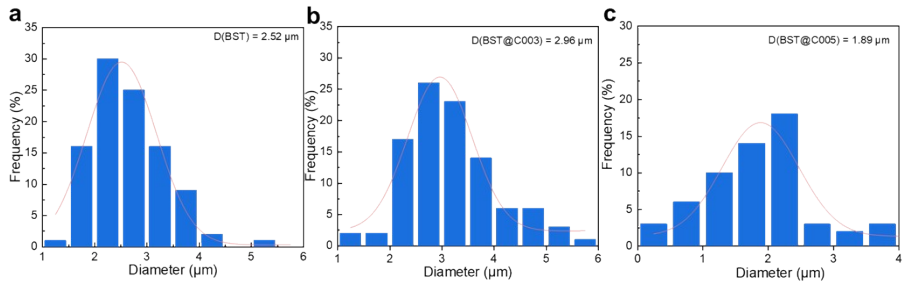

Figure S5. (a-c) Grain size of sintered pristine BST, BST@C003, and C005 bulk samples.

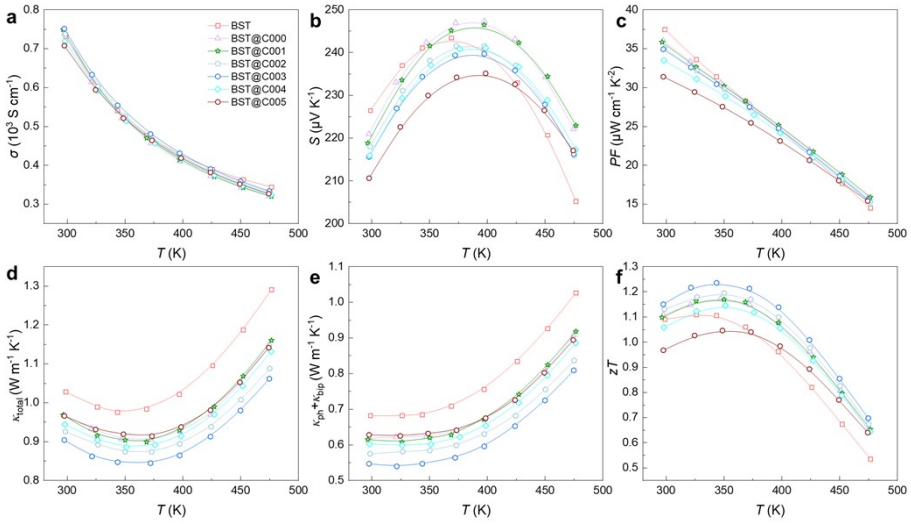

Figure S6. Thermoelectric properties of pristine BST and BST@C000 – BST@C005 bulk samples parallel to the pressure direction. **(a)** Temperature dependence of the σ; **(b)** temperature dependence of the S; **(c)** temperature dependence of the PF; **(d)** temperature dependence of the κ; **(e)** temperature dependence of the $\kappa_L+\kappa_{bip}$; and **(f)** temperature dependence of the zT.

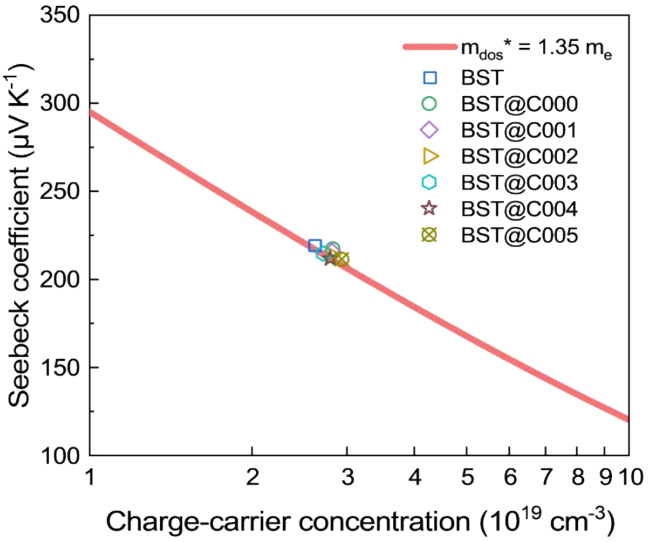

Figure S7. Pisarenko plot against experimental Seebeck coefficients as a function of measured charge-carrier concentration at 300 K.

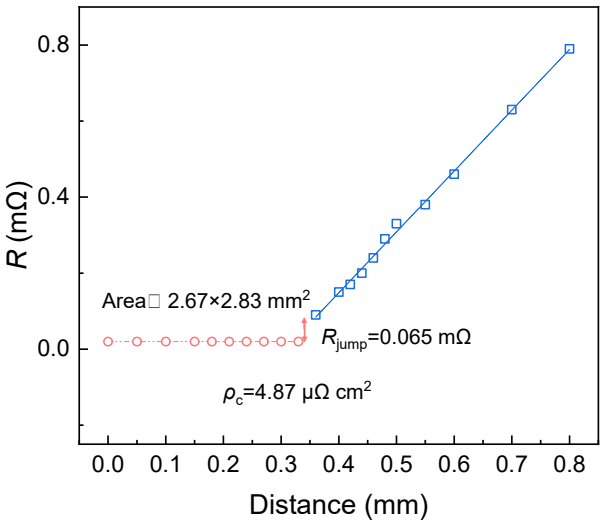

Figure S8. Thermoelectric properties and the contact resistance of n-type Bi_2Te_3 legs.

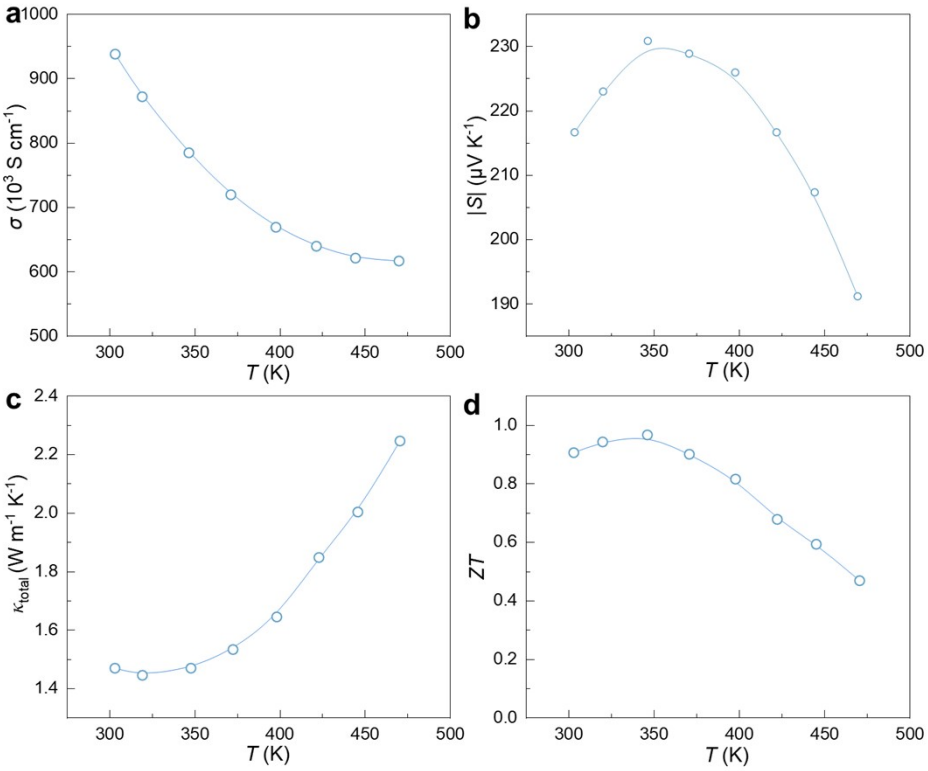

Figure S9. Thermoelectric properties of the commercial n-type $Bi_2Te_3Se_{0.3}$ materials used in the cooling module.

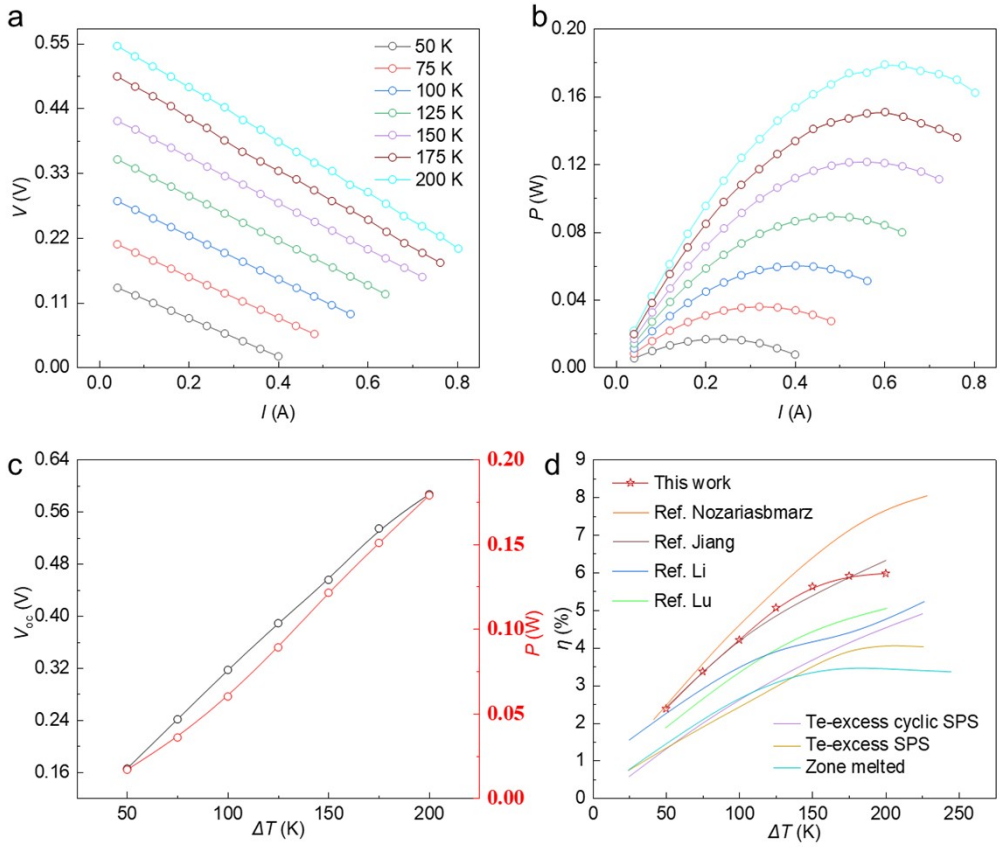

Figure S10. Performance of the power-generation module. (a) Output voltage, **(b)** output power, **(c)** V_{oc} and P_{max} as a function of temperature difference, **(d)** the corresponding conversion efficiency at different temperature gradients compared to literature studies.[9–13]

Table S1. Crystallographic information based on the Rietveld refinement against PXRD datasets.

Chemical Formula	**Pristine BST**	**BST@C003**	**BST@C005**
Crystal System	Trigonal	Trigonal	Trigonal
Space Group	$R\bar{3}m$	$R\bar{3}m$	$R\bar{3}m$
Lattice parameters/ Å（α	a = 4.289645(99)	a = 4.289643(101)	a =4.290586 (141)
= β=90°, γ = 120°）	c = 30.460482(821)	c = 30.457138(681)	c = 4.290586 (1195)
Cell volume/ Å	485.412 (27)	485.358 (26)	485.686 (39)
Formula weight/g mol^{-1}	1984.753	1982.748	1988.601
Formula units, Z	3	3	3
No. of observations	3961	4951	4951
χ^2	3.023	2.674	2.745
R_p	0.0596	0.0560	0.0637
wR_p	0.0787	0.0754	0.0822

Table S2. Atomic parameters of the pristine BST sample based on the Rietveld refinement.

Atom	***Wyckoff* symbol**	***x***	***y***	***z***	**100****Uiso*/ Å² **(Equivalent)**	**Occupancy**
Bi	*6c*	0	0	0.398987(49)	1.903	0.25
Sb	*6c*	0	0	0.398987(49)	1.903	0.716
Te1	*6c*	0	0	0.211598(34)	1.659	1
Te2	*3a*	0	0	0	1.505	1

Table S3. Atomic parameters of the BST@C003 sample based on the Rietveld refinement.

Atom	***Wyckoff* symbol**	***x***	***y***	***z***	**100****Uiso*/ Å² **(Equivalent)**	**Occupancy**
Bi	*6c*	0	0	0.399045(41)	2.987	0.25
Sb	*6c*	0	0	0.399045(41)	2.987	0.713
Te1	*6c*	0	0	0.211531(29)	2.690	1
Te2	*3a*	0	0	0	2.540	1

Table S4. Atomic parameters of the BST@C005 sample based on the Rietveld refinement.

Atom	***Wyckoff* symbol**	***x***	***y***	***z***	**100****Uiso*/ Å² **(Equivalent)**	**Occupancy**
Bi	*6c*	0	0	0.399009 (72)	2.289	0.25
Sb	*6c*	0	0	0.399009 (72)	2.289	0.721
Te1	*6c*	0	0	0.211645 (87)	2.006	1
Te2	*3a*	0	0	0	1.807	1

Table S5. Parameters for the calculation of κ_{ph} of the pristine BST and BST@C003 samples in the Debye-Callaway model.

Parameter	Description	Value	Method
θ_D	Debye temperature	94 K	[9]
B_D	Effective Burger's vector	1.2×10^{-9} m	fitted
v_l	Longitudinal sound velocity	3622 m s^{-1}	Calculated
v_T	Transverse sound velocity	2133 m s^{-1}	Calculated
v	Average speed of sound	2344 m s^{-1}	Calculated
γ	Grüneisen parameter	2.33	[14]
r	Poisson's ratio	0.196	Calculated
V	Average atomic volume of $Bi_{0.5}Sb_{1.5}Te_3$	31.26 $Å^3$	[15]
V_{BT}	Atomic volume of Bi_2Te_3	3.4×10^{-29} m^3	[15]
V_{ST}	Atomic volume of Sb_2Te_3	3.31×10^{-29} m^3	[14]
M_{BT}	Atomic mass of Bi_2Te_3	2.79×10^{-29} kg	[9]
M_{ST}	Atomic mass of Sb_2Te_3	2.07×10^{-29} kg	[9]
C_0	Concentration of $Bi_{0.5}Sb_{1.5}Te_3$ in Bi_2Te_3	0.25	[16]
K	Bulk modulus	45.8 Gpa	Calculated
T_a	Sintering temperature	639 K	Exp.
d	Grain size	2.52/2.96 μm	Exp.
N_d	Dislocation density	3×10^{11} cm^{-2}	Exp.
R	Average radius of second phase	5 nm	Exp.
N_P	Number density of Second phase	3.0×10^{22} m^3	Exp. and evaluation
D	Density of matrix	6.68/6.65 gcm^{-3}	Exp.

Supplementary references

[1] Allen PB. Improved Callaway model for lattice thermal conductivity. Phys Rev B 2013;88:144302. https://doi.org/10.1103/PhysRevB.88.144302.

[2] Bailyn M. Transport in Metals. II. Effect of the Phonon Spectrum and Umklapp Processes at High and Low Temperatures. Phys Rev 1960;120:381–404. https://doi.org/10.1103/PhysRev.120.381.

[3] Carlson RO, Slack GA, Silverman SJ. Thermal Conductivity of GaAs and GaAs1− *x* P *x* Laser Semiconductors. Journal of Applied Physics 1965;36:505–7. https://doi.org/10.1063/1.1714018.

[4] Klemens PG. Phonon scattering and thermal resistance due to grain boundaries. Int J Thermophys 1994;15:1345–51. https://doi.org/10.1007/BF01458842.

[5] Shindé SL, Goela JS, editors. High Thermal Conductivity Materials. New York: Springer-Verlag; 2006. https://doi.org/10.1007/b106785.

[6] Guo Z, Roy Chowdhury P, Han Z, Sun Y, Feng D, Lin G, et al. Fast and accurate machine learning prediction of phonon scattering rates and lattice thermal conductivity. Npj Comput Mater 2023;9:95. https://doi.org/10.1038/s41524-023-01020-9.

[7] Hu L, Meng F, Zhou Y, Li J, Benton A, Li J, et al. Leveraging Deep Levels in Narrow Bandgap $Bi_{0.5}$ $Sb_{1.5}$ Te_3 for Record-High zT_{ave} Near Room Temperature. Adv Funct Materials 2020;30:2005202. https://doi.org/10.1002/adfm.202005202.

[8] Goldsmid HJ. Introduction to Thermoelectricity. vol. 121. Berlin, Heidelberg: Springer Berlin Heidelberg; 2016. https://doi.org/10.1007/978-3-662-49256-7.

[9] Pang K, Yuan M, Zhang Q, Li Y, Zhang Y, Zhou W, et al. High Performance Thermoelectric Power of $Bi_{0.5}$ $Sb_{1.5}$ Te_3 Through Synergistic Cu_2 $GeSe_3$ and Se Incorporations. Small 2024;20:2306701. https://doi.org/10.1002/smll.202306701.

[10] Lu T, Wang B, Li G, Yang J, Zhang X, Chen N, et al. Synergistically enhanced thermoelectric and mechanical performance of Bi2Te3 via industrial scalable hot extrusion method for cooling and power generation applications. Materials Today Physics 2023;32:101035. https://doi.org/10.1016/j.mtphys.2023.101035.

[11] Nozariasbmarz A, Poudel B, Li W, Kang HB, Zhu H, Priya S. Bismuth Telluride Thermoelectrics with 8% Module Efficiency for Waste Heat Recovery Application. iScience 2020;23:101340. https://doi.org/10.1016/j.isci.2020.101340.

[12] Cai B, Zhuang H-L, Pei J, Su B, Li J-W, Hu H, et al. Spark plasma sintered Bi-Sb-Te alloys derived from ingot scrap: Maximizing thermoelectric performance by tailoring their composition and optimizing sintering time. Nano Energy 2021;85:106040. https://doi.org/10.1016/j.nanoen.2021.106040.

[13] Zhuang H-L, Hu H, Pei J, Su B, Li J-W, Jiang Y, et al. High *ZT* in p-type thermoelectric $(Bi,Sb)_2$ Te_3 with built-in nanopores. Energy Environ Sci 2022;15:2039–48. https://doi.org/10.1039/D2EE00119E.

[14] Zhang Q, Yuan M, Pang K, Zhang Y, Wang R, Tan X, et al. High-Performance Industrial-Grade p-Type $(Bi,Sb)_2$ Te_3 Thermoelectric Enabled by a Stepwise Optimization Strategy. Advanced Materials 2023;35:2300338. https://doi.org/10.1002/adma.202300338.

[15] Toberer ES, Zevalkink A, Snyder GJ. Phonon engineering through crystal chemistry. J Mater Chem 2011;21:15843. https://doi.org/10.1039/c1jm11754h.

[16] Ikeda T. Nanostructured Bulk Thermoelectric Materials. Materia Japan 2014;53:307–11. https://doi.org/10.2320/materia.53.307.